OPEN ACCESS

KING'S College LONDON

King's Research Portal

DOI:
10.1021/acs.jctc.5b01236

Document Version
Peer reviewed version

Link to publication record in King's Research Portal

Citation for published version (APA):
Suardíaz, R., Jambrina, P. G., Masgrau, L., González-Lafont, À., Rosta, E., & Lluch, J. M. (2016). Understanding the Mechanism of the Hydrogen Abstraction from Arachidonic Acid Catalyzed by the Human Enzyme 15-Lipoxygenase-2. A Quantum Mechanics/Molecular Mechanics Free Energy Simulation. *Journal of Chemical Theory and Computation*, *12*(4), 2079-2090. https://doi.org/10.1021/acs.jctc.5b01236

Citing this paper
Please note that where the full-text provided on King's Research Portal is the Author Accepted Manuscript or Post-Print version this may differ from the final Published version. If citing, it is advised that you check and use the publisher's definitive version for pagination, volume/issue, and date of publication details. And where the final published version is provided on the Research Portal, if citing you are again advised to check the publisher's website for any subsequent corrections.

General rights
Copyright and moral rights for the publications made accessible in the Research Portal are retained by the authors and/or other copyright owners and it is a condition of accessing publications that users recognize and abide by the legal requirements associated with these rights.

•Users may download and print one copy of any publication from the Research Portal for the purpose of private study or research.
•You may not further distribute the material or use it for any profit-making activity or commercial gain
•You may freely distribute the URL identifying the publication in the Research Portal

Take down policy
If you believe that this document breaches copyright please contact librarypure@kcl.ac.uk providing details, and we will remove access to the work immediately and investigate your claim.

Download date: 16. Aug. 2022

Understanding the Mechanism of the Hydrogen Abstraction from Arachidonic Acid Catalyzed by the Human Enzyme 15-Lipoxygenase-2. A Quantum Mechanics/Molecular Mechanics Free Energy Simulation.

Reynier Suardíaz,[1] Pablo G. Jambrina,[1] Laura Masgrau,[2] Àngels González-Lafont,[2,3,*] Edina Rosta,[1,*] and José M. Lluch[2,3]

[1]Department of Chemistry, King's College London, London SE1 1DB, United Kingdom

[2]Institut de Biotecnologia i de Biomedicina (IBB), Universitat Autònoma de Barcelona, 08193 Bellaterra, Barcelona, Spain

[3]Departament de Química, Universitat Autònoma de Barcelona, 08193 Bellaterra, Barcelona, Spain

ABSTRACT

Lipoxygenases (LOXs) are a family of enzymes involved in the biosynthesis of several lipid mediators. In the case of human 15-LOX, the 15-LOX-1 and 15-LOX-2 isoforms show slightly different reaction regiospecificity and substrate specificity, indicating that substrate binding and recognition may be different, a fact that could be related to their different biological role. Here, we have used long molecular dynamics simulations, QM(DFT)/MM potential energy and free energy calculations (using the newly developed DHAM method), to investigate the binding mode of the AA substrate into 15-LOX-2 and the rate-limiting hydrogen-abstraction reaction 15-LOX-2 catalyzes. Our results strongly indicate that hydrogen abstraction from C13 in 15-LOX-2 is only consistent with the "tail-first" orientation of AA, with its carboxylate group interacting with Arg429, and that only the pro-S H13 hydrogen will be abstracted (being the pro-R H13 and H10 too far from the acceptor oxygen atom). At the B3LYP/6-31G(d) level the potential and free energy barriers for the pro-S H13 abstraction of AA by 15-LOX-2 are 18 and 18.6 kcal/mol, respectively. To analyze the kinetics of the hydrogen abstraction process, we determined a Markov model corresponding to the unbiased simulations along the state-discretized reaction coordinate. The calculated rates based on the second largest eigenvalue of the Markov matrices agree well with experimental measurements, and also provide the means to directly determine the pre-exponential factor for the reaction by comparing with the free energy barrier height. Our calculated pre-exponential factor is close to the value of k_BT/h. Our results suggest that

the spin inversion of the complete system (including the O_2 molecule) that is required to happen at some point along the full process to lead to the final hydroperoxide product, is likely to take place during the hydrogen transfer, which is a proton coupled electron transfer. Overall, a different binding mode from the one accepted for 15-LOX-1 is proposed, which provides a molecular basis for 15-LOX-2 exclusive 15-HPETE production in front of the double (although highly 15-) 12/15 regiospecificity of 15-LOX-1. Understanding how these different isoenzymes achieve their regiospecificity is expected to help in specific inhibitor design.

KEYWORDS

Human enzyme 15-lipoxygenase-2; rate-limiting hydrogen-abstraction reaction; regiospecificity; Quantum Mechanics/Molecular Mechanics calculations; Dynamics Histogram Analysis Method.

1. INTRODUCTION

Lipoxygenases (LOXs) are a family of non-heme, non-sulfur iron dioxygenases that catalyze the peroxidation of the 1,4-*Z*-*Z*-pentadiene units of polyunsaturated fatty acids.[1,2] The fatty acid hydroperoxides formed by the different LOX isoenzymes are the starting points for the biosynthesis of a number of lipid mediators involved in many relevant cell processes and human pathologies.[3-7]

The rate-determining step of the complete hydroperoxidation reaction is an initial hydrogen atom abstraction from a bisallylic methylene group of the fatty acid substrate by the Fe(III)-OH^- moiety that precedes the addition of molecular oxygen to the fatty acid and the subsequent retro-hydrogen transfer to the peroxy radical (Figure 1).[4,8] These reactions are highly specific. Accordingly, animal LOXs are classified on the basis of the position of hydroperoxidation on the substrate arachidonic acid (AA).[5,8-12] There are 6 available carbon atoms in AA that can be attacked by molecular oxygen, and specific animal LOXs exist for 5 of them (5-, 8-, 11-, 12- and 15-LOX).[5,13] This specificity is extremely relevant because the different LOX metabolites often exert opposing biological effects, and high specificity is therefore required. For instance, 5-LOX converts AA to the pro-inflammatory leukotrienes. Conversely, the combined action of first 15-LOX and then 5-LOX leads to the synthesis of lipoxins that are involved in the resolution phase of inflammation.[5]

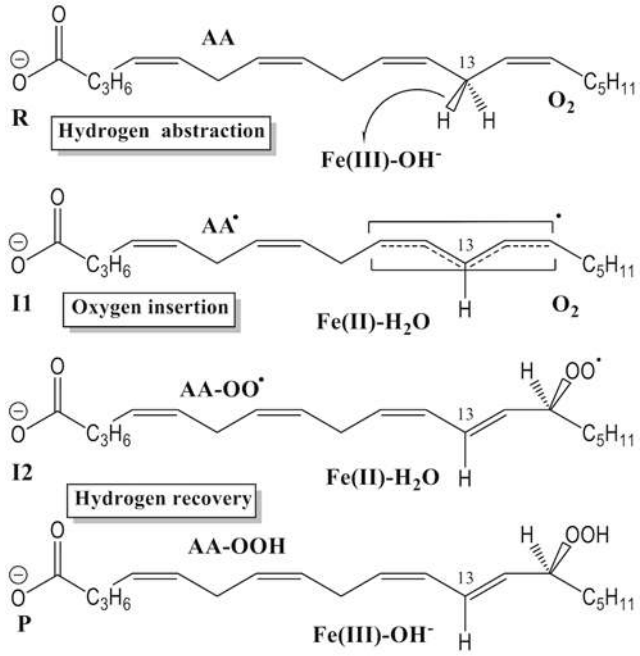

Figure 1: The three reaction steps of hydrogen abstraction, oxygen insertion and hydrogen recovery are drawn with the corresponding structures (reactant, R, intermediate I1 and I2, and product P).

One of the most important LOX enzymes is 15-LOX. There are two human LOXs, with less than 40% sequence identity, that hydroperoxidate AA at position 15: reticulocyte 15-LOX-1 and epithelial 15-LOX-2.[14,15] In spite of the chemically analogous mechanism to oxidize AA at the same carbon atom 15, their biological role is distinctly different.[16] On the other hand, 15-LOX-1 preferentially metabolizes linoleic acid primarily to 13-hydroperoxyoctadecadienoic acid (13-HPODE), but also catalyzes the conversion of AA mainly to 15-hydroperoxyeicosatetraenoic acid (15-HPETE) and, in a lesser extent, to 12-hydroperoxyeicosatetraenoic acid (12-HPETE).[15,16] Conversely, 15-LOX-2 metabolizes linoleic acid poorly and converts AA exclusively to 15-HPETE.[16] In addition, based on crystallographic structures with an inhibitor positioned as a substrate mimic, a so-called U-shaped substrate binding cavity has been assumed in human 15-LOX-2, but a boot-shaped was derived in rabbit 15-LOX-1 that has approximately 80% sequence identity with human 15-LOX-1.[2] Holman and coworkers[17] have suggested that binding and recognition for human 15-LOX-2 are fundamentally different from that of human 15-LOX-1. This could explain the difference in their substrate specificity. In particular, they have performed the AA docking to a human 15-LOX-2 homology model built using the rabbit 15-LOX-1 crystallographic structure and found a salt bridge between the carboxylate group of AA and Arg429. However, the long distance (over 17 Å) between Arg429 and the active site did not allow proper positioning of AA for hydrogen atom abstraction, with an unlikely position of the methyl end of the substrate near the iron atom. In contrast to human 15-LOX-1, there were no positively charged residues in the vicinity of the human 15-LOX-2 active site to facilitate binding of the carboxylate group of AA.

The apparently opposite biological function between the two 15-LOXs warrants the development of specific inhibitors of these isoforms. To this aim, a detailed knowledge of their respective mechanisms at the molecular level and a comparison between them

is highly desirable. In recent years we devoted significant effort to theoretically study the 15-LOX-1 enzyme and its catalytic mechanism.[18-23] In particular, we have recently carried out quantum mechanics/molecular mechanics (QM/MM) calculations to study the hydrogen abstraction reaction from AA catalyzed by rabbit 15-LOX-1.[24] We have shown that, in good agreement with the experimental results, most of the products of this reaction arise from the initial hydrogen abstraction from the carbon C13 of AA, although hydrogen abstraction from C10 is also possible. Moreover, we have found that there exist a wide range of geometries of the AA:15-LOX-1 Michaelis complexes in a suitable position to transfer one of the hydrogen atoms to the acceptor oxygen atom of the cofactor Fe(III)-OH^- and likewise a wide range of the corresponding potential energy barriers.

This paper is aimed at understanding how the human enzyme 15-Lipoxygenase-2 manages to catalyze the hydrogen abstraction from arachidonic acid in a highly regio- and stereospecific way. To this purpose we have combined molecular dynamics simulations, QM/MM calculations, and Umbrella Sampling free energy simulations using the very recently developed dynamic histogram analysis method (DHAM),[25] which is not only able to provide the free energies, but also the kinetic rate of the reaction. We also determined the pre-exponential factor for the reaction using the free energy barrier height and the calculated kinetic rate. The comparison with the enzyme 15-Lipoxygenase-1 is also presented.

2. COMPUTATIONAL METHODS

2.1. Initial coordinates

The complex AA:15-LOX-2 structure is based on the 4NRE crystal structure recently available in the Protein Data Bank.[15] The newly reported structure has a substrate mimic bound at the active site of the protein occupying the position expected for arachidonic acid (AA), the natural substrate of the enzyme. This crystallized inhibitor has the same number of atoms as AA and similar flexibility. This crystal structure therefore provides a good model for the positioning of the substrate within the active site, but details about the precise orientation are missing. Hence, we considered three possible orientations: i) “head-first” (carboxylate group pointing to the core of the protein); ii) “tail-first" (carboxylate group pointing to the surface) with the pro-S H13 in a reactive position; and iii) “tail-first" with the pro-R H_{13} in a reactive position. On the other hand, Newcomer and coworkers [2, 15] have suggested that formation of 15-HPETE (arising from abstraction at C13 in AA) is only consistent with the tail-first entry of AA.

In the crystallographic structure there are two water molecules coordinating the iron atom. This situation differs from most of the reported structures of 15-lipoxygenases that have only a single coordinating water molecule.[26-29] We analysed the electron density map (Figure S1 in SI) from the structure factors deposited in the PDB under the 4NRE code using the PHENIX software.[30] According to this map, the region with the second water molecule (801 in PDB file) could also be occupied by the side chain of Ser557. Therefore, we tested a second model where the oxygen atom of the Ser557 side chain coordinates the iron instead of the water molecule. As will be shown below, the fact that a water or Ser557 coordinates the iron, does not considerably affect the H abstraction reaction.

2.2. Molecular dynamics simulations

Hydrogen coordinates were generated with standard protonation states for all ionisable residues using CHARMM.[31] The system was solvated with a pre-equilibrated TIP3 cubic water box of 116 $Å^3$. Water molecules were randomly replaced by ions to ensure the neutralization of the system, and an additional KCl salt concentration corresponding to 0.15 M. The resulting system contains 147471 atoms, including the

water molecules. For all the three possible orientations mentioned above, we carried out 10000 steps of energy minimization and then molecular dynamics (MD) simulations using periodic boundary conditions (PBC). The production trajectories were run for 100 ns after 1 ns of equilibration using NAMD.[32] A time step of 2 fs was used. Temperature and pressure were held constant at 300 K and 1 atm, respectively. All of the bonds and angles involving hydrogen atoms were constrained by the SHAKE[33] algorithm. We used the CHARMM36[34] force field, and the particle mesh Ewald method[35] for the long range electrostatics in combination with a 12 Å cutoff for the evaluation of the non-bonded interactions.

2.3. QM/MM calculations

Once the system was classically equilibrated, it was trimmed to a sphere of 20 Å radius centred at the AA. Atoms further than 15 Å from the AA were kept frozen during all the QM/MM calculations. No cutoffs were introduced for the non-bonding MM and QM/MM interactions. We have used Q-Chem v4.1[36,37] and Gaussian09 rD01[38] program packages to perform the all-electron QM calculations using the B3LYP functional with or without the D3 version of Grimme's dispersion correction[39,40] and in combination with the 6-31G(d), 6-31G(d,p), 6-31+G(d), 6-311G(d) or 6-311+G(d,p) basis sets. The quantum mechanical system was coupled with the CHARMM program[31] for the MM region. A full electrostatic embedding scheme[41] has been adopted in all the calculations and hydrogen link atoms have been used to treat the QM/MM boundaries. The reaction paths were scanned by performing restrained geometry optimizations along the reaction coordinate $z = r_1(C13\text{-}H13) - r_2(H13\text{-}O)$ (see Figure 2), using a step size of 0.2 Å both in the forward and backward directions to obtain hysteresis-free results.[42] The QM region for all geometry optimizations encloses all the 50 atoms depicted in red in Figure 2, including the AA from C10 to C16, the Fe atom (all electrons), part of the side chains of His373, His378, His553 and Ile676, one water molecule (or Ser557 side chain; 52 atoms in this case) and the catalytic hydroxide anion.

2.4. Sequence alignments

Alignments were performed using the default parameters of the ClustalΩ[43] algorithm via the Uniprot[44] portal.

2.5. Free energy calculations

Umbrella sampling free energy calculations were performed to compute the potential of mean force (PMF) and the 2D free energy profile along the reaction coordinate. We used the same level of theory, B3LYP/6-31G(d), and QM region (Figure 2) as described above. 20 umbrella windows were run placing harmonic biasing potentials along the reaction coordinate at steps of 0.2 Å ($-1.6 \leq z \leq 2.0$ Å with $z = r_1 - r_2$) using a spring constant of 250 kcal/(mol Å^2). The QM/MM dynamics in each window was run for at least 6 ps after equilibration using a Langevin thermostat and a time step of 1 fs.

Two alternative algorithms were used to calculate the free energies. We used a high-precision implementation of the dynamic histogram analysis method (DHAM)[25] to calculate the free energies and the kinetic rate of the reaction. We also evaluated the free energies using a binless implementation (MBAR)[45-47] of the weighted histogram analysis method (WHAM).[48,49]

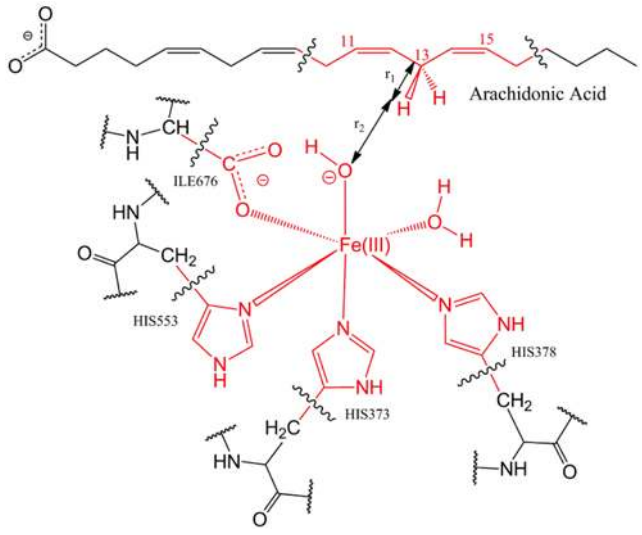

Figure 2. Schematic view of the QM/MM partition. The QM atoms are depicted in red, the boundary between the QM and MM regions is indicated by wavy lines. The reaction coordinate is defined as a function of the r_1 and r_2 distances.

3. RESULTS AND DISCUSSION

3.1. Ligand orientation

The newly reported crystal structure has an inhibitor bound at the active site of the protein. This crystallized ligand was replaced by AA taking advantage of the similarities in the molecular constitution and flexibility. As recognized by Newcomer and coworkers, the resolution of the electron density map does not allow the precise determination of the orientation even for the crystallized inhibitor.[15] Hence, we considered two possible orientations: “head-first” and “tail-first” (Figure 3). We also took into account two possible conformations of AA in the “tail-first” orientation: one positioned for the abstraction of the pro-S H13 and one favouring the abstraction of the pro-R H13.

i) “head-first” orientation: The carboxylate group of the ligand points to the core of the protein and is directly facing Val426, Val427 and Ile420 hydrophobic residues. This aliphatic non-polar environment seems unsuitable for binding of the charged carboxylate end of AA. Accordingly, our MD simulations showed that the carboxylate group is unstable in this binding mode and it moves away towards the protein surface (see Figure S2). Once the head of AA reaches the surface, the position of the fatty acid is stabilized due to the carboxylate group’s interactions with the surrounding solvent waters.

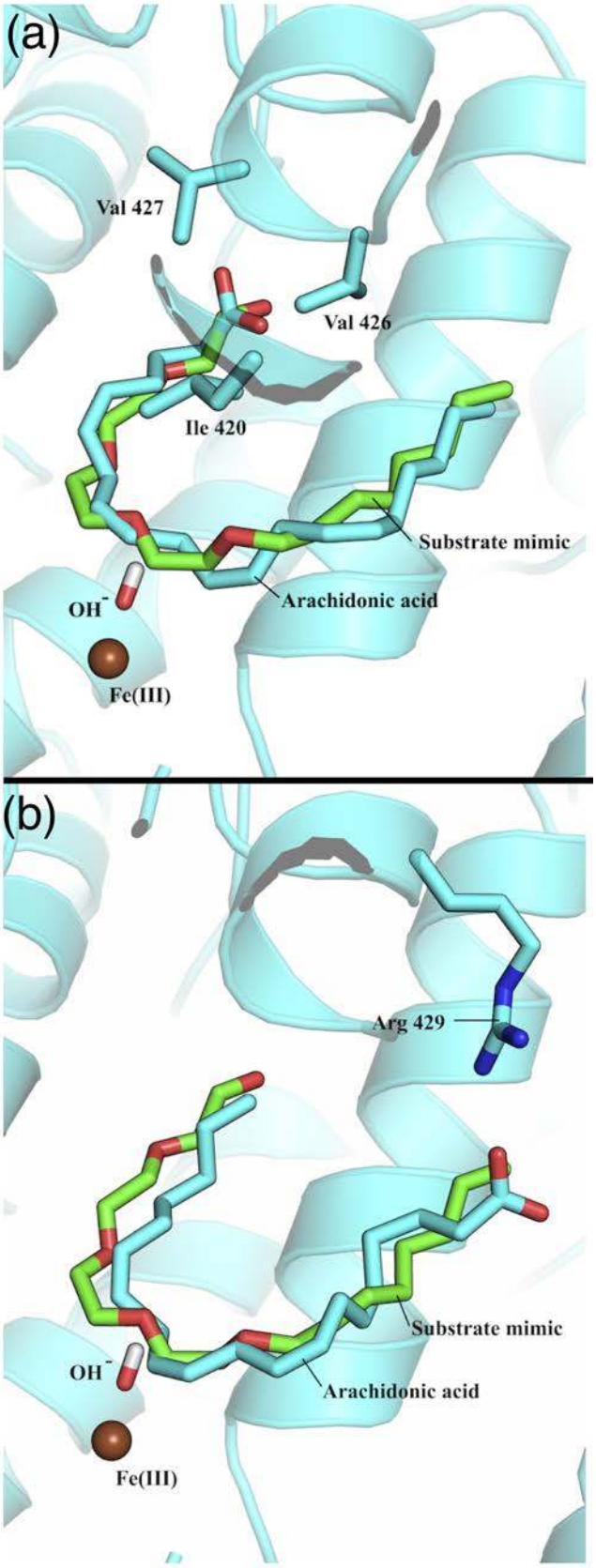

Figure 3: Licorice representation of the original inhibitor crystallized with the protein (C in green, O in red) replaced by AA (C in light blue, O in red). a) “head-first” orientation,

also highlighting interactions with Val426, Val427 and Ile420 hydrophobic residues. b) “tail-first” orientation, also highlighting interactions with Arg429.

ii) “tail-first orientation” with the pro-S H13 in a reactive position: In this position, the carboxylate group of AA directly interacts with Arg429. This strong interaction between two oppositely charged groups stabilizes the position of AA inside the binding pocket. During the 100 ns long MD simulations, AA moves between two conformations. The first conformation corresponds to the one observed for the inhibitor in the crystal structure and it is perfectly positioned for the abstraction reaction, as the H13 of AA is located very close to the hydroxide ion (Figure S3, green, in SI). The second conformation occurs following a twist in the first moiety of the fatty acid (C1 to C7) resulting in an even stronger interaction with the Arg429. This conformer corresponds to an unproductive H abstraction position, due to the larger, over 5 Å, distance of carbon positions 13 and 10 (Figure S3, cyan, in SI) to the acceptor oxygen, and the large distance between the hydroxide ion and the hydrogen atoms of C13.

Figure 4a shows the time evolution of the distances between the oxygen of the hydroxide anion and the nearest H atoms, pro-S H13 and pro-S H10, that can potentially be abstracted. According to the MD simulation, and based on the distances, AA stays most of the time in the “non-reactive” conformation and eventually comes back to the conformation able to start H-abstraction. We have used the data produced in this simulation to estimate the free energies corresponding to the distances data shown in Figure 4a. According to the free energy plots shown in Figure 4b, there are two well-defined populations for the O-H13 distances data, one of them corresponding to a small minimum at approximately 2.5 Å (distance pro-S H13 - O), and the other one corresponding to a minimum at ~4.8 Å. For the O-H10 distances data, there is only one populated minimum where pro-S H10 is located at around 4.5 Å away from O. As the distance from the OH group to the pro-S H10 is quite large in both conformations, (“productive” and “unproductive”), it is very unlikely that the H-abstraction reaction occurs in this position. This would be the reason why 15-LOX-2 metabolizes AA

exclusively to 15-HPETE, the abstraction in C10 (needed for the formation of 12-HPETE) not being accessible. On the other hand, the conformation of the substrate based in the crystal, which coincides with one of the populated conformations in our MD simulations, locates the pro-S H13 at a distance short enough from the hydroxide anion to be the abstracted hydrogen. Hence, based on the actual structure of 15-LOX-2, our simulations confirm that the carboxylate group of AA interacts with Arg429, as also found previously by Holman and coworkers[17] who showed that AA is positioned in a catalytically competent way for the pro-S H13 abstraction to happen.

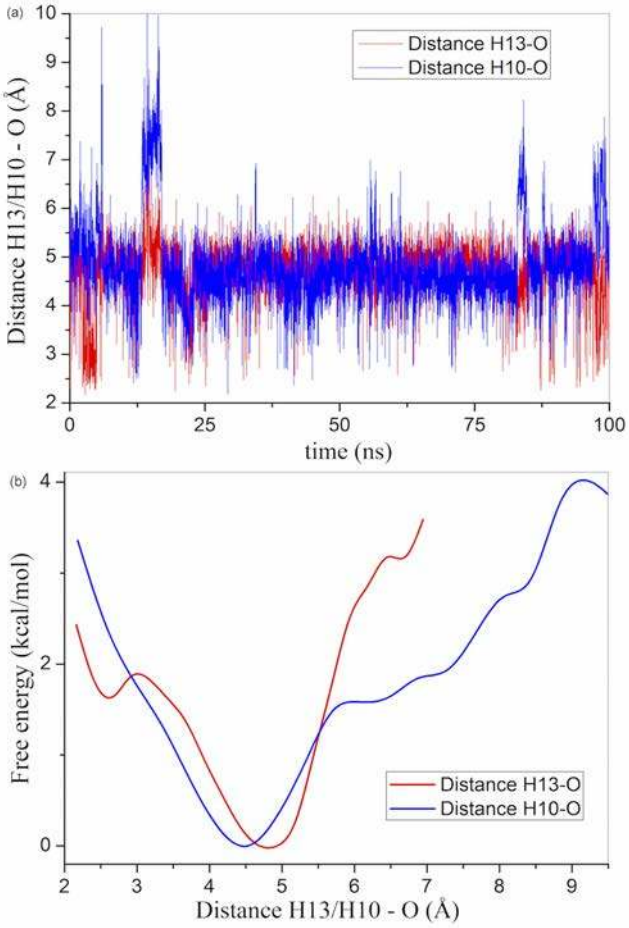

Figure 4: a) Distances from the oxygen of the hydroxide to the AA pro-S H13 (blue) and pro-S H10 (red) during the MD simulation. b) Free energy profiles obtained from the MD data at 300 K using DHAM.

iii) "tail-first orientation" with the pro-R H13 in a reactive position: In this orientation, the carboxylate group of AA interacts directly with Arg429 as in the previous

orientation. However, the conformation of AA has been changed to favor the abstraction of the pro-R H13. When the pro-R H13 points to the OH^-, AA loses, in some extent, the so-called "U shape" needed for the proper accommodation inside the binding pocket. This twisted conformation is not stable, and after no more than 2 ns of MD simulations the AA converges to the conformation ii with the pro-S H13 pointing towards the hydroxide group.

Thus, our results show that hydrogen abstraction from C13 of AA by 15-LOX-2 is only consistent with the "tail-first" orientation of AA, and also that only the pro-S H13 will be abstracted.

3.2. Binding mode of human 15-LOX-2 in comparison to rabbit 15-LOX-1

Our MD results suggest that AA accommodates in the active site of 15-LOX-2 with a "tail-first" orientation and its position seems to strongly depend on the interaction with Arg429. It is worth mentioning that, in rabbit 15-LOX-1 (and presumably in human 15-LOX-1) there is also an Arginine residue (Arg403) defining the position of AA inside the protein.[50] This Arginine residue is conserved in mammalian, including human, 15-LOX-1 enzymes, however it is not conserved in the human 15-LOX-2 enzyme (Table 1). In fact, the equivalent residue in human 15-LOX-2 is a Leucine. Adjacent to this Leu415 in 15-LOX-2 there are two other residues, Thr414 and Ala416. Consequently, we propose that AA binds to the human 15-LOX-2 in a different binding mode than in mammalian 15-LOX-1 enzymes. At the same time, in mammalian 15-LOX-1 the amino acids corresponding to Arg429 in 15-LOX-2 are negatively charged (Asp) or Gln, Ile or Val depending on the organism. This also strongly suggests that the binding modes of AA in the 15-LOX-1 and 15-LOX-2 enzymes are significantly different.

Furthermore, comparison of the structures of rabbit 15-LOX-1 and human 15-LOX-2 makes apparent that the binding of AA in 15-LOX-2 does not require the conformational change that has been proposed for 15-LOX-1.[2,15,28,51] In fact, the 15-LOX-2:AA structure is very similar to the apo 15-LOX-1 one. One of the differences observed between the two ligand-bound structures is that the helix α18 fills a larger part of the binding site cavity in 15-LOX-2:AA (see Figure 5). As a consequence of that, for example, the minimum C-C distance between hLeu420 and hLeu610 (rLeu408 and

rLeu597), two residues important in binding AA, is of ~8 and ~4 Å in 15-LOX-1 and 15-LOX-2, respectively. This restrains the ligand motion and could contribute to a more rigid binding of AA in 15-LOX-2.

(a)

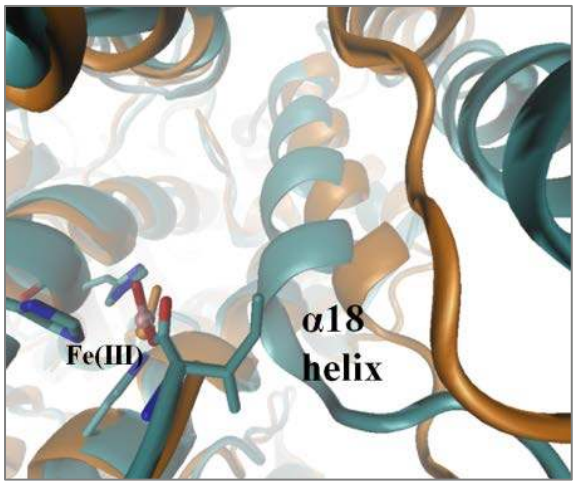

(b)

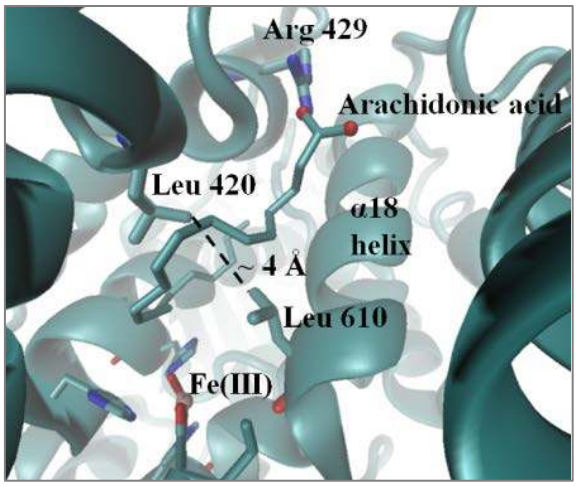

(c)

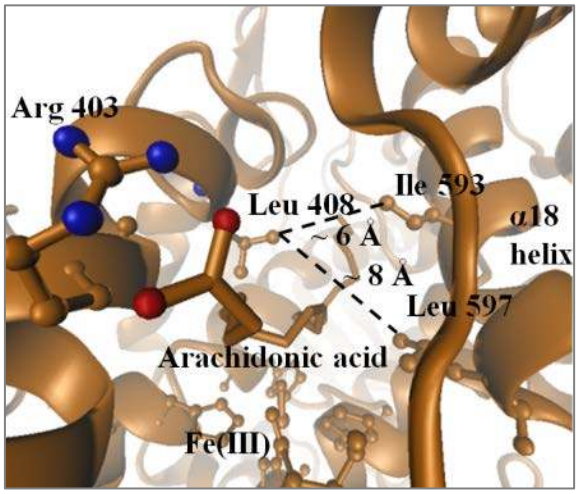

Figure 5: Comparison of the 15-LOX-1[51] (orange) and 15-LOX-2 (cyan) complexes with the AA substrate. Structures taken from molecular dynamics simulations of models built based on crystallographic data.[15,28] (a) Differences in the conformation adopted by the α18 helix, which modulates the space available in the active site. As an example, the (b) Leu420 – Leu610 distance (15-LOX-2:AA), and (c) the equivalent Leu408 – Leu597 distance (15-LOX-1:AA) are shown. The location of Ile593 with respect to Leu408 is also indicated.

Interestingly, two water molecules coordinate the iron atom in the human 15-LOX-2 crystallographic structure.[15] This is different from all the reported structures of mammalian 15-lipoxygenase structures, which have only a single water molecule (or hydroxide group) coordinating the Fe atom.[26-29,50,51] We considered the possibility of an alternative assignment of the observed density at the position of the second water molecule as the nearby Ser557 group. However, our results do not indicate significant differences in the reaction profiles regarding this assignment (see SI for further details).

Table 1. Sequence alignment of human 15-LOX-2 with mammalian 15-LOX-1 isoforms. In red, key Arg residues are highlighted interacting with bound AA in 15-LOX. In blue, equivalent residues that occupy approximately the same space as those Arg residues.

414	T	L	A	R	E	L	L	I	V	P	G	Q	V	V	D	R	S	430	HUMAN 15-LOX-2
402	V	R	A	R	N	G	L	V	S	D	F	G	I	F	D	Q	I	418	RABBIT 15-LOX-1
401	V	R	A	R	T	G	L	V	S	D	M	G	I	F	D	Q	I	417	HUMAN 15-LOX-1
401	V	R	A	R	T	G	L	V	S	D	M	G	I	F	D	Q	I	417	PONAB 15-LOX-1
402	V	R	A	R	N	G	L	V	S	D	L	G	I	F	D	Q	V	418	PIG 15-LOX-1
402	I	R	A	R	T	G	L	V	S	D	S	G	V	F	D	Q	V	418	BOVIN 15-LOX-1

3.3. Reaction energy profiles

After the classical equilibration of the system in the "tail-first" orientation with the pro-S H13 in a reactive position (the only orientation that stays stable along the MD simulation), a snapshot belonging to the free energy well centered at a pro-S H13-O distance of 2.5 Å (see Figure 4b) was chosen and a full QM/MM geometry optimization was performed. The QM region included the iron atom (all electrons), part of the aminoacid side chains coordinating the iron, the hydroxide group and part of the AA acid as described in the Methods section and in Figure 2. The optimized geometry was used as the starting point for the potential energy reaction profile. The reaction path was scanned by performing partial geometry optimizations along the reaction coordinate defined by $z = r_1(C13\text{-}H13) - r_2(H13\text{-}O)$ (Figure 2). The potential energy reaction profile was initially calculated at the B3LYP/6-31G(d) level (Figure 6a, green line), using backward and forward minimizations until convergence was achieved.[42] The barrier height for human 15-LOX-2 obtained in this work at the B3LYP/6-31G(d) level is 18.0 kcal/mol (see Figure 6a). This potential energy barrier is similar to the one reported recently for a set of potential energy reaction paths corresponding to the abstraction of H13 in rabbit 15-LOX-1.[24] The reaction is exoergic by approximately 7 kcal/mol. The reactants lie at approximately z=-1.2 Å and the products at 1.2 Å. The transferred hydrogen is equidistant to the H-donor and acceptor in the transition state structure at z= 0.0 Å.

To account for potentially missing thermal and entropic contributions, we computed the free energy profile using Umbrella Sampling. Biased QM/MM molecular dynamics simulations were performed for at least 6ps on each umbrella window at the B3LYP/6-31G(d) level using the same QM region as previously defined (see more information in SI). Here we have used the recently developed DHAM method[52] to calculate both the free energies as well as the kinetic rate corresponding to the catalytic reaction. We used a new high precision Matlab implementation of the DHAM method[52] to allow us to numerically obtain accurate free energy profiles for the reaction with a high free energy barrier where the largest eigenvalues of the Markov matrix are almost

degenerate. We calculated the Markov matrices corresponding to the unbiased transition probabilities of the system at three different lag times, 1 fs, 10 fs, and 50 fs and determined their spectral decompositions (Table S2 in SI). The slowest relaxation rate corresponding to the second largest eigenvalue was consistent between the three lag times considered, and provided an average rate constant of 0.22 ± 0.05 s^{-1}. The fact that the calculated rates obtained at different lag time values are very similar (see Table S2 in SI) indicates that our choice of reaction coordinate describes well the kinetically important degrees of freedom for the catalytic process. The free energy barrier using the DHAM method was found to be 18.6 ± 0.5 kcal/mol (see Figure 6a), very similar to the potential energy barrier, thus indicating that thermal and entropic contributions to the free energy are small. We have also calculated the unidimensional free energy profile using the traditional WHAM method with a binless implementation (MBAR) for comparison with DHAM (see Figures 6a and 6b). Moreover, a two-dimensional free energy surface as a function of the coordinates r_1 and r_2, the two components of the reaction coordinate z, has been calculated using the WHAM method (see Figure 6b). All methodologies give roughly identical results.

At this point, it can be noted that, according to Canonical Variational Transition-State Theory,[53,54] the free energy barrier (ΔG^{CVT}) is related to the rate constant by means of the equation

$$k(T) = \Gamma \frac{k_B T}{h} e^{-\frac{\Delta G^{CVT}}{RT}} \qquad \text{(eq. 1)}$$

where k is the rate constant, T is the temperature, k_B is Boltzmann's constant, h is Plank's constant, R is the gas constant, and Γ is the quassiclassical transmission factor that corrects the rate constant for dynamical recrossing through the dividing surface corresponding to the canonical variational transition (CVT) state (that is, where the generalized transition-state free energy of activation is maximum). The frequency factor k_BT/h equals 6.3×10^{12} s^{-1} at T=300 K, but the calculation of Γ is not easy. The advantage of using the DHAM method is that, at least at an approximate level, the barrier-crossing times can be estimated directly from the global analysis of local Umbrella Sampling trajectories, so that the effect of the dynamical recrossing is incorporated. Thus, the entire pre-exponential factor in eq.1 can be obtained

substituting in that equation the rate constant and the free energy barrier calculated by the DHAM method, leading to a value of approx. 7.8×10^{12} s^{-1} at 300 K, remarkably close to the value of $k_B T/h$. Thus, the dynamical recrossing is not significant in this case at the CVT dividing surface.

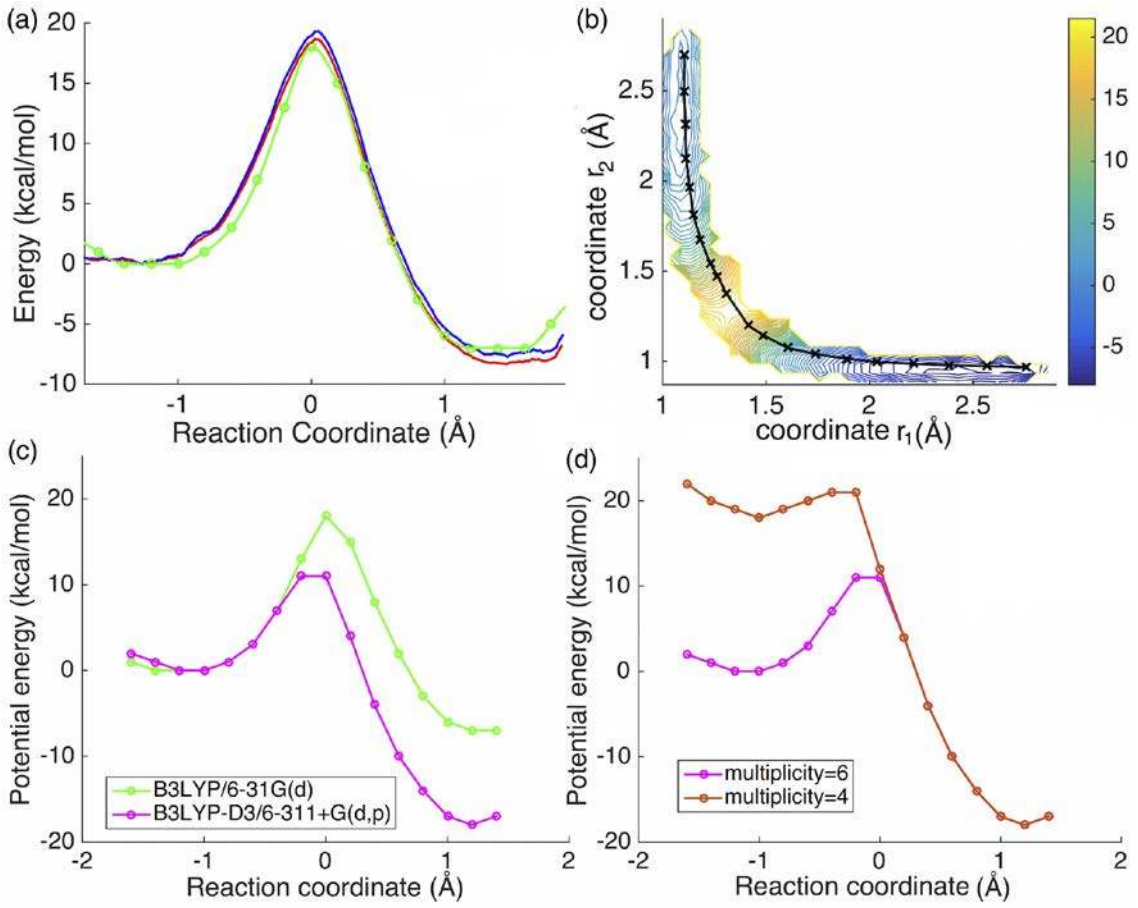

Figure 6: a) Potential energy (green) and free energy profiles (blue-WHAM, red-DHAM) calculated at the B3LYP/6-31G(d) level of theory. b) 2D-Free energy surface obtained by the WHAM method. c) Potential energy profiles calculated at the B3LYP/6-31G(d) (green) and B3LYP-D3/6-311+G(d,p) (pink) levels of theory. d) Potential energy profiles calculated at the B3LYP-D3/6-311+G(d,p) level with multiplicity 6 (pink) and multiplicity 4 (orange).

To test how sensitive is the potential energy barrier to the electronic structure level used, we also calculated the fully optimized potential energy profile at a higher level of theory. Both the potential energy barrier height and the reaction energy change are

considerably lower when a higher level of theory including additional diffuse and polarization basis functions is used (Figure 6c). A decrease in the barrier height of around 6 kcal/mol and 10 kcal/mol in the reaction energy is obtained at the B3LYP-D3/6-311+G level. Nevertheless, if we use an even larger basis set like cc-pVQZ (quadruple-ζ) to perform single point calculations over the already obtained geometries, we get a barrier height of 16.6 kcal/mol (see Figure S8 in SI). Furthermore, if we use a mixture of the aug-cc-pV5Z (quintuple-ζ) basis set for the atoms directly involved in the reaction (methylene group containing the transferred H, hydroxyl group receiving the transferred H and Fe atom) and the triple-ζ basis set already used (6-311+G(d,p)) for the rest of the atoms to perform the single point calculations, we get a reaction barrier height of 16.2 kcal/mol. These results indicate that the decrease in the barrier height when used the 6-311+G(d,p) could be overrated. We performed additional calculations at different levels of theory using B3LYP with and without D3 Grimme's dispersion correction in combination with the 6-31G(d), 6-31G(d,p), 6-31+G(d), 6-311G(d) or 6-311+G(d,p) basis sets (see SI).

The entropic contribution to the reaction is expected to be very small based on our free energy calculations (Figure 6a). We note that the system was trimmed to a sphere of 20 Å radius centred at the AA. Recent work indicated that this might contribute to the fact that the entropy contributions remain small, although the free energies are nevertheless consistent.[55,56] In the present particular case, once the reactive structure with the pro-S H13 near the oxygen acceptor atom is chosen, the evolution to the transition state is rather a local phenomenon for the first reaction step. Binding of the oxygen molecule in the second step could incur a large entropy change, and additional protein rearrangements after the product formation are also expected to give larger entropy changes. Thus, we estimate that the exclusion of the outside part of the protein for the first reaction step should be a good approximation in this specific case. The similarity between the potential energy profile and the free energy profile has been previously found in the hydrogen abstraction from linoleic acid catalyzed by soybean lipoxygenase-1.[57] We also expect similar free energy and potential energy values at the higher level of theory. The results at the B3LYP-D3/6-311+G level of

theory have been used for the subsequent analysis of spin states and electronic structure.

The sensitivity of the barriers to the electronic structure level of calculation opens an interesting point to be discussed. Using the 6-31G(d) basis set, the DHAM method directly uses Umbrella Sampling simulations to give a rate constant of 0.22 ± 0.05 s^{-1}. The experimental results obtained by Holman and coworkers[17,58] are 0.74 ± 0.03 s^{-1} or 1.5 ± 0.03 s^{-1} at 22 °C and pH=7.5. The excellent agreement turns out to be quite impressive, but it could actually be somewhat fortuitous. As seen above, a barrier 6 kcal/mol lower would be predicted at the B3LYP-D3/6-311+G level of theory, a value that breaks the nice concordance with experiments. However, single point calculations using an even larger basis set like cc-pVQZ only lower the potential energy barrier 1.4 kcal/mol with respect to the 6-31G(d) value. At this point we should be aware that the current state-of-the-art of both, experiments and theory, does not allow the direct comparison between the respective rate constants (measured vs. calculated) in the present case (and for many other enzyme reactions) for several reasons:

1) Experimental rates[17,58] were determined spectrophotometrically by following the formation of the conjugate diene product of hydroperoxidation at 234 nm. To the best of our knowledge, no direct measure of the rate of the hydrogen abstraction exists.

2) Sometimes a more extended basis set is not balanced enough to warrant necessarily better results for this kind of systems. For instance, the inclusion of diffuse functions on Fe could be a poor match when used with the underlying 6-31G or 6-311G basis sets.[59]

3) As seen in Figure 4, along the 100 ns molecular dynamics simulation many structures with the pro-S H13 near the oxygen acceptor atom (and then ready to transfer) appear, but most of the structures have H13 too far to contribute to the abstraction (that is, the corresponding abstraction would involve quite high barriers). As a matter of fact, we should randomly select a huge number of snapshots along the MD simulation, calculate the hydrogen abstraction barriers starting from each of them, and average the corresponding rate constants.[60] However, this procedure would involve a computational effort beyond our current capabilities. The choice of one (or a

few) snapshots, just the one (or ones) more prone to produce the reaction is evident that biases the result towards lower barriers, so overestimating the rate constants.

To summarize this point, the results obtained in this paper are reasonable and provide useful, reliable, and detailed information at the molecular level about the catalytic mechanism that human 15-LOX-2 employs to abstract a hydrogen atom from AA. However, the state-of-the-art of the methods is not mature enough to give accurate values of the rate constants of these enzyme reactions yet.

On the other hand, in this work we have not taken into account the quantum nature of the hydrogen atom that is transferred. However, we think that inclusion of quantum mechanical tunneling would not significantly change the main qualitative trends of this hydrogen transfer reaction catalyzed by human 15-LOX-2 that we have described here.

3.4. Spin states

There is a strong experimental evidence that the iron is in its high spin state in the active, ferric form of lipoxygenases.[61] For that reason we have performed most of our calculations using multiplicity M= 6, corresponding to a closed shell arachidonic acid and a high spin ferric ion in the reactants. Nevertheless, we have also calculated the potential energy profile with M= 4. Multiplicity 2 corresponds to the significantly less stable low spin state of the ferric iron and the M= 4 is plausible for the products of the reaction as will be clarified below. The possible spin states along each step of the reaction (see Figure 1) are illustrated in Figure 7. We refer to the multiplicity of both the current system considered in this work (not including the oxygen molecule, boxed in red in Figure 7), and also to the full system including the oxygen molecule needed for the subsequent reaction steps (boxed in blue in Figure 7). In the reactants (R in Figures 1 and 7) the multiplicity of the current system is 6, considering that the iron is in the high spin state. With the oxygen included, the system could have M= 8 or 4. After H abstraction (I1 structure in Figures 1 and 7) the system can go through various spin multiplicity states, but in the products the only possible one is M=6 since the only

atom bearing unpaired electron would be the recovered ferric iron (P in Figures 1 and 7). As the possible multiplicities in the reactants were 8 or 4, there must be a change of spin state during the course of the full reaction. According to the reaction profiles obtained in this work, that change of spin state could occur in the first rate-limiting step of the reaction, from 6 to 4 (without including the oxygen), where the B3LYP-D3/6-311G+(d,p) potential energy profiles with M=6 and 4 become degenerate after the transition state of the hydrogen abstraction step (Figure 6d). If the iron were more stable in a low spin state a spin crossover would not be necessary, since the multiplicity of the system could be 2 over the entire reaction (Figure 7, bottom). Note that the spin state of the low spin iron is not exactly the same in P and R (the unpaired electron spin is inverted), but that does not mean that a spin inversion is required. Nevertheless, as already mentioned, there is strong experimental evidence that the iron is in its high spin state. Therefore we suggest that, according to our calculations, the multiplicity of the reactants would be 8 or 4 (6 without including the oxygen), and both would be equally likely since the oxygen molecule doesn't need to be close to the reaction center at this step. After H-abstraction, the probability of (i) to remain in the M=6 state or (ii) to change one electron spin at M=4 is the same due to the near degenerate energies, however the choice of (ii) would lead to the final product directly, without additional spin inversion. Any other choice would require a further spin inversion to reach the final product multiplicity state during subsequent steps.

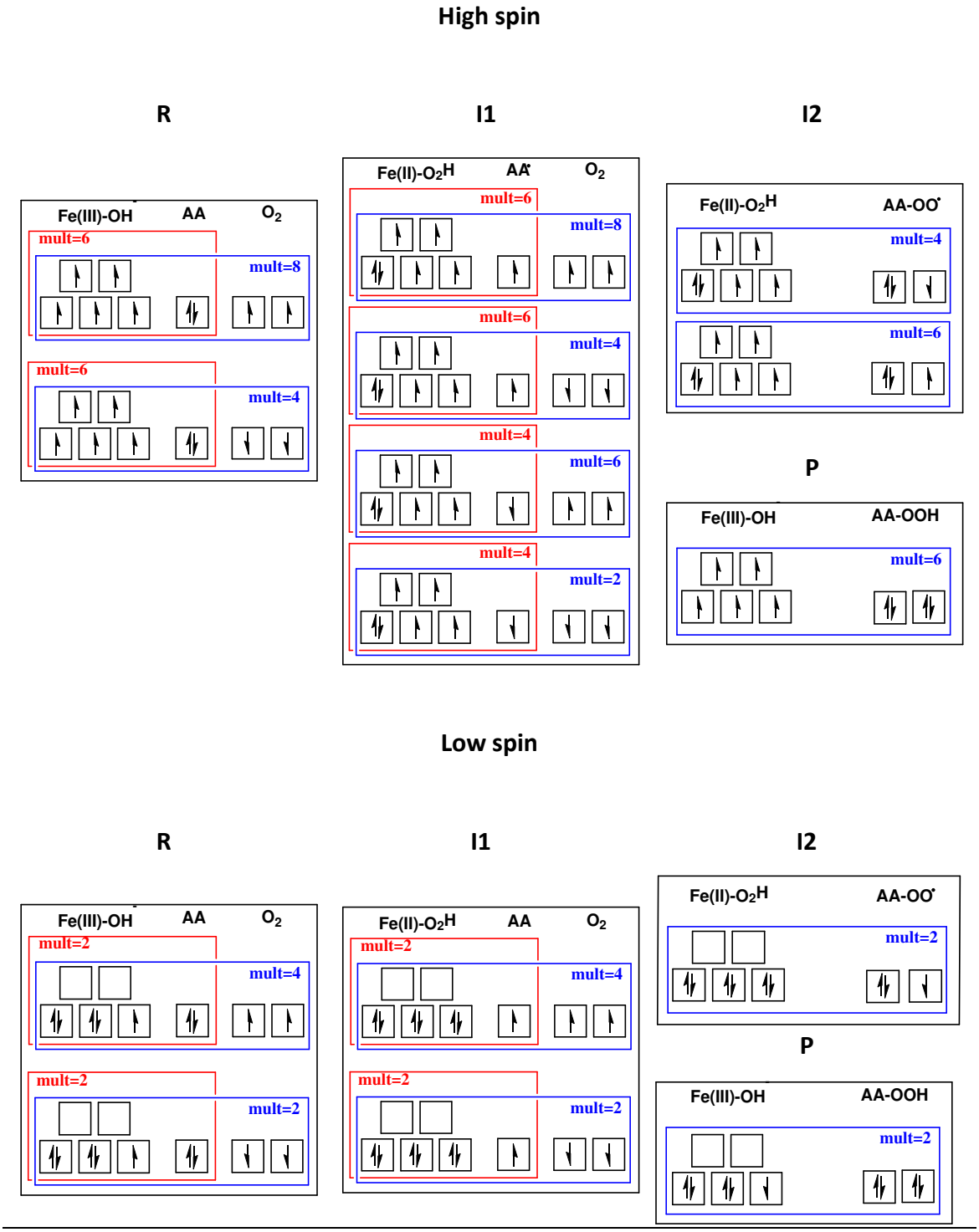

Figure 7: Possible spin multiplicity states of the system during the complete hydroperoxidation reaction. Boxed in red, the system studied in this work (that is, without considering the oxygen); the full system, boxed in blue.

3.5. Electronic structure analysis

Atomic populations evaluated from the spin density, indicating the excess of α spin have been calculated along the potential energy profiles at the same level of theory B3LYP-D3/6-311+G(d,p) with multiplicities 6 and 4. Figure 8 shows the evolution during the H-abstraction reaction on the carbon atoms C11, C12, C13, C14 and C15 of the pentadienyl system of AA, the abstracted pro-S H13 atom and the Fe. As the H13 is being abstracted by the hydroxide group, the spin density on C13 increases and delocalizes over C11 and C15, up to half an electron in each atom. The spin densities on C12 and C14 change from 0 to approximately -0.3 a.u. The sum over all carbon atoms is approximately one unpaired electron spread over the pentadienyl radical system. The spin density on the Fe atom changes from approximately 4.2 to 3.7 a.u., which corresponds to the change of the oxidation state from Fe(III) sextet to Fe(II) quintet configuration. The spin density on the H13 remains virtually zero during the reaction, which suggests that the transferred hydrogen is rather a proton not bearing any electron. Spin density isosurfaces along the reaction pathway are shown in Figure 9. On the other hand, the H13 atom is positively charged during the reaction course (magenta line in Figure 8) with the charge changing from 0.25 to 0.5 a.u., confirming that this atom is in fact a proton. The analysis of the evolution of the electronic structure along the H abstraction shows that the reaction corresponds to a proton coupled electron transfer (PCET) process,[62-68] in which the electron and proton are transferred in a concerted way. The proton is transferred to the OH−group oxygen to form water, whereas the electron is transferred from the AA C11−C15 pentadiene moiety to the Fe(III) atom to produce Fe(II).

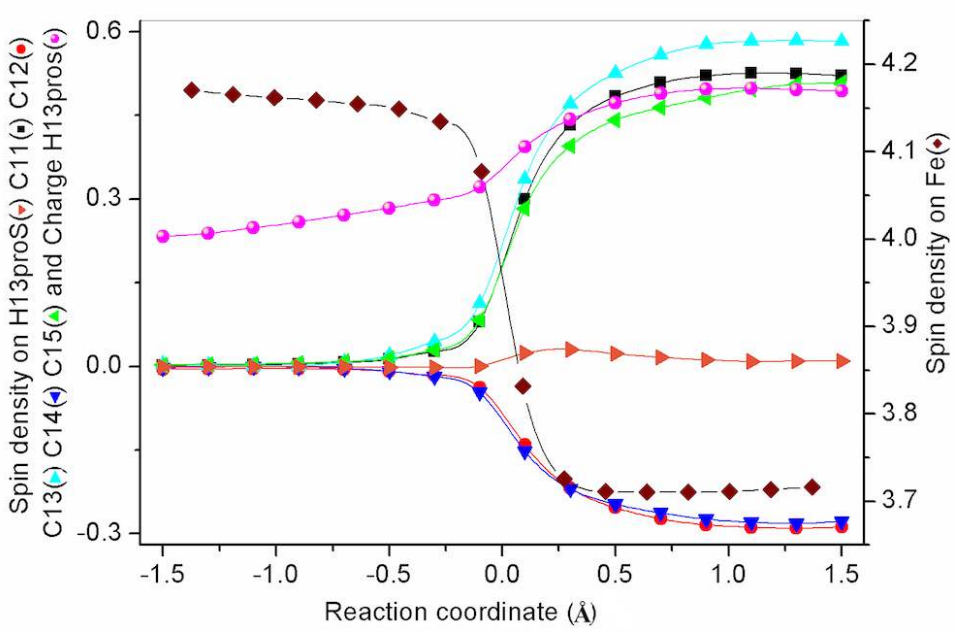

Figure 8: Spin densities (a.u.) on atoms pro-S H13 (orange), C11(black), C12(red), C13(cyan), C14(blue), C15(green) and Fe(brown) along the H-abstraction reaction. In magenta, the charge (a.u.) of pro-S H13 along the reaction is given.

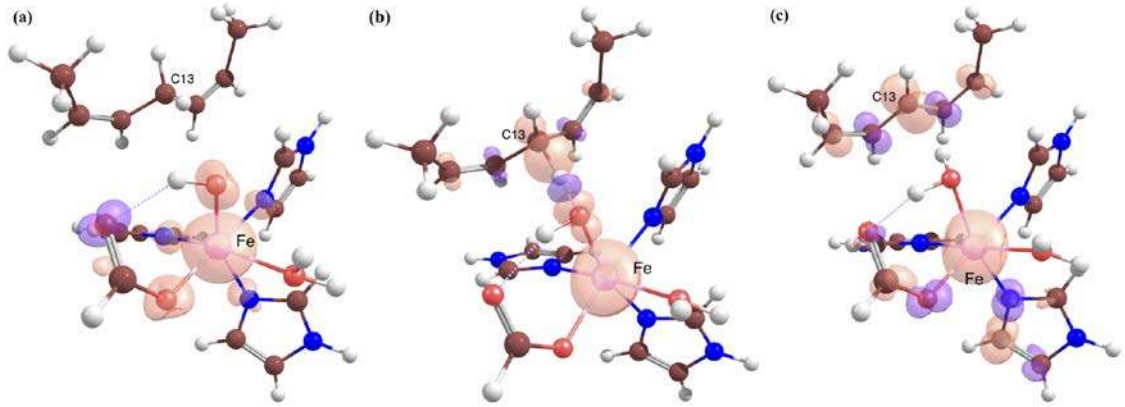

Figure 9: Spin density surfaces in the reactants (a), transition state structure (b) and products (c).

An NBO analysis[69] at the transition state structure shows a simultaneous bonding pattern between the H donor (C13) and the H acceptor (O) since the bond order (via Wiberg bond index) is around 0.4 for C13-H13 and H13-O. Also, the analysis of the occupancy of α electrons shows that there is almost one electron (occupancy = 0.92)

occupying the σ(bonding) orbital of the C13-H13 bond. Nevertheless, as for β electrons, the populated (occupancy = 0.88) σ(bonding) is H13-O. Figure 10 shows the relevant occupied orbitals in the reactants, transition state structure and products.

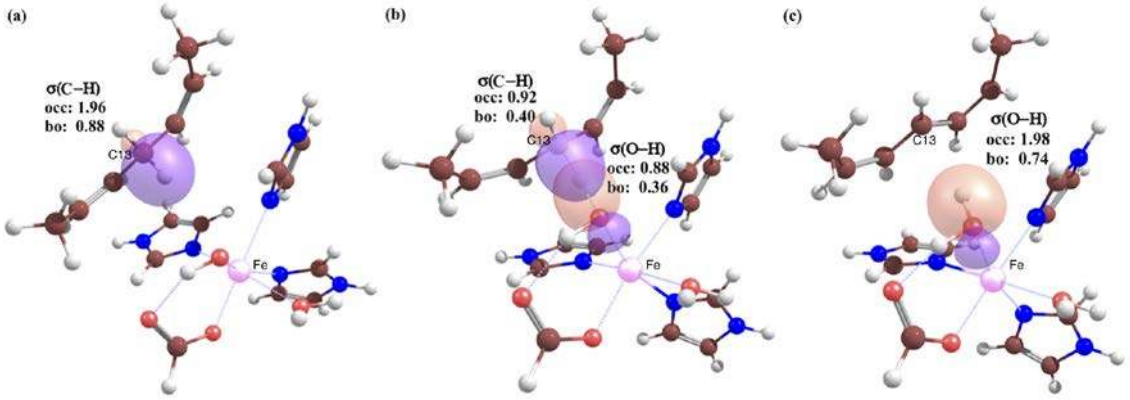

Figure 10: Evolution of selected natural bond orbitals at reactants (a) transition state structure (b) and products (c). Occupancies (occ) and bond orders (bo) are labeled in each case.

4. CONCLUSIONS

In this paper we have combined molecular dynamics simulations, QM/MM calculations and Umbrella Sampling free energy simulations to study the hydrogen atom abstraction from arachidonic acid catalyzed by the human enzyme 15-lipoxygenase-2.

The orientation of AA inside the active site of the enzyme cannot be determined from the electron density of the crystallographic structure[15], but it may be a key aspect to better understand the regiospecificity of the different LOXs isoforms. Our molecular dynamics simulations show that the "head-first" orientation of AA is unstable. Instead, we have confirmed that when AA adopts a "tail-first" orientation, its carboxylate group clearly interacts with Arg429 and many structures ready for the pro-S H13 abstraction appear. Conversely, the pro-R H13 is not placed in a suitable conformation to be abstracted.

The hydrogen atoms in position 10 remain most of the time too far from the acceptor oxygen atom to compete with H13 abstraction. This fact can explain why human 15-LOX-2 metabolizes AA exclusively to 15-HPETE, 12-HPETE not being produced.

The fact that the "tail-first" orientation of AA strongly depends on the interaction with Arg429 indicates that the binding modes of AA in human 15-LOX-2 and mammalian 15-LOX-1 are significantly different. Moreover, the binding of AA is more rigid in human 15-LOX-2 than in rabbit 15-LOX-1.

At the B3LYP/6-31G(d) level the potential energy barrier for the pro-S H13 abstraction of AA by human 15-LOX-2 is 18 kcal/mol. Performing Umbrella Sampling simulations along with either the very recently developed dynamic histogram analysis method (DHAM)[52] or the WHAM[48] method, a free energy barrier of 18.6 kcal/mol has been obtained, indicating that thermal and entropic contributions to the free energy barrier are small in this case. DHAM calculations also provide directly the catalytic rate constant and show that the dynamical recrossing is negligible at the canonical variational transition state. This is the first time that the kinetics is determined directly from biased umbrella sampling simulations using the DHAM method for catalytic reactions, allowing also the estimation of the pre-exponential factor for the reaction.

The above electronic structure calculations correspond to a multiplicity M=6, that is, a closed shell for AA and a high spin ferric ion in the reactants. Multiplicity M=4 is significantly more unstable than M=6 in the reactants, but both spin states become nearly degenerate after the transition state of the hydrogen abstraction. As a consequence, we propose that the spin inversion of the complete system (including the O_2 molecule) that is required to happen at some point along the full process to lead to the final hydroperoxide product, is likely to take place during the hydrogen transfer.

Finally, the hydrogen transfer occurs by means of a proton coupled electron transfer (PCET) mechanism, in which the electron and the proton are transferred in a concerted way to different atomic centers.

ACKNOWLEDGEMENTS

E. R. is gratefully acknowledges Dr. Gerhard Hummer for helpful discussions about the DHAM method. R.S. acknowledges the FEBS for a short-term fellowship, the EC for a Marie Curie IEF fellowship (project number 622711) and the Alianza 4U program. R.S., L.M., A.G. and J.M.L. thank the Spanish "Ministerio de Economía y Competitividad" (Grant CTQ2014-53144-P) for financial support. L.M. acknowledges the support from the "UAB-Banco de Santander" program. We acknowledge computer time on ARCHER granted via the UK High-End Computing Consortium for Biomolecular Simulation, HECBioSim (http://hecbiosim.ac.uk), supported by EPSRC (grant no. EP/L000253/1) and the computational resources of the NIH biowulf cluster.

SUPPORTING INFORMATION

Supporting information includes an electron density map for the area close to Fe atom, initial and last geometries of "head-first" and "tail-first" orientations of AA along the MD simulations, two "tail-first" conformations of AA inside the active site, rmsd values along the simulation trajectories, additional information about the umbrella sampling simulation, information about kinetic data obtained from DHAM method, the effect of the electronic structure level in reaction energy profiles, and a discussion on the

possible presence of Ser557 instead of water coordinating Fe. This material is available free of charge via the Internet at http://pubs.acs.org

REFERENCES

(1) Kuhn, H.; Banthiya, S.; van Leyen, K. *Biochim. Biophys. Acta, Mol. Cell Biol. Lipids* **2015**, *1851*, 308.

(2) Newcomer, M. E.; Brash, A. R. *Protein Sci.* **2015**, *24*, 298.

(3) Dobrian, A. D.; Lieb, D. C.; Cole, B. K.; Taylor-Fishwick, D. A.; Chakrabarti, S. K.; Nadler, J. L. *Prog. Lipid Res.* **2011**, *50*, 115.

(4) Haeggström, J. Z.; Funk, C. D. *Chem. Rev.* **2011**, *111*, 5866.

(5) Joo, Y.-C.; Oh, D.-K. *Biotechnol. Adv.* **2012**, *30*, 1524.

(6) Abrial, C.; Grassin-Delyle, S.; Salvator, H.; Brollo, M.; Naline, E.; Devillier, P. *Br. J. Pharmacol.* **2015**, *172*, 4319.

(7) Palermo, G.; Bauer, I.; Campomanes, P.; Cavalli, A.; Armirotti, A.; Girotto, S.; Rothlisberger, U.; De Vivo, M. *PLoS Comput Biol* **2015**, *11*, e1004231.

(8) Ivanov, I.; Heydeck, D.; Hofheinz, K.; Roffeis, J.; O'Donnell, V. B.; Kuhn, H.; Walther, M. *Arch. Biochem. Biophys.* **2010**, *503*, 161.

(9) Schneider, C.; Pratt, D. A.; Porter, N. A.; Brash, A. R. *Chem. Biol.* **2007**, *14*, 473.

(10) Coffa, G.; Brash, A. R. *Proc. Natl. Acad. Sci. U. S. A.* **2004**, *101*, 15579.

(11) Schwarz, K.; Walther, M.; Anton, M.; Gerth, C.; Feussner, I.; Kuhn, H. *J. Biol. Chem.* **2001**, *276*, 773.

(12) Vogel, R.; Jansen, C.; Roffeis, J.; Reddanna, P.; Forsell, P.; Claesson, H.-E.; Kuhn, H.; Walther, M. *J. Biol. Chem.* **2010**, *285*, 5369.

(13) Eek, P.; Järving, R.; Järving, I.; Gilbert, N. C.; Newcomer, M. E.; Samel, N. *J. Biol. Chem.* **2012**, *287*, 22377.

(14) Jameson, J. B., II; Kantz, A.; Schultz, L.; Kalyanaraman, C.; Jacobson, M. P.; Maloney, D. J.; Jadhav, A.; Simeonov, A.; Holman, T. R. *PLoS One* **2014**, *9*, e104094.

(15) Kobe, M. J.; Neau, D. B.; Mitchell, C. E.; Bartlett, S. G.; Newcomer, M. E. *J. Biol. Chem.* **2014**, *289*, 8562.

(16) Hsi, L. C.; Wilson, L. C.; Eling, T. E. *J. Biol. Chem.* **2002**, *277*, 40549.

(17) Wecksler, A. T.; Kenyon, V.; Deschamps, J. D.; Holman, T. R. *Biochemistry* **2008**, *47*, 7364.

(18) Suardíaz, R.; Masgrau, L.; Lluch, J. M.; González-Lafont, À. *J. Phys. Chem. B* **2013**, *117*, 3747.

(19) Suardiaz, R.; Masgrau, L.; Lluch, J. M.; Gonzalez-Lafont, A. *ChemPhysChem* **2014**, *15*, 2303.

(20) Suardiaz, R.; Masgrau, L.; Lluch, J. M.; Gonzalez-Lafont, A. *ChemPhysChem* **2013**, *14*, 3777.

(21) Suardiaz, R.; Masgrau, L.; Gonzalez-Lafont, A.; Lluch, J. M. *FEBS J.* **2013**, *280*, 94.

(22) R. Suardiaz, L. M., J. M. lluch, À. González-Lafont *FEBS J.* **2014**, *281*, 636.

(23) Suardíaz, R.; Masgrau, L.; Lluch, J. M.; González-Lafont, À. *ChemPhysChem* **2014**, *15*, 4049.

(24) Saura, P.; Suardíaz, R.; Masgrau, L.; Lluch, J. M.; González-Lafont, À. *ACS Catal.* **2014**, *4*, 4351.

(25) Rosta, E.; Hummer, G. *J. Chem. Theory Comput.* **2015**, *11*, 276.

(26) Garreta, A.; Val-Moraes, S. P.; García-Fernández, Q.; Busquets, M.; Juan, C.; Oliver, A.; Ortiz, A.; Gaffney, B. J.; Fita, I.; Manresa, À.; Carpena, X. *FASEB J.* **2013**, *27*, 4811.

(27) Gillmor, S. A.; Villasenor, A.; Fletterick, R.; Sigal, E.; Browner, M. F. *Nat Struct Mol Biol* **1997**, *4*, 1003.

(28) Choi, J.; Chon, J. K.; Kim, S.; Shin, W. *Proteins: Struct., Funct., Bioinf.* **2008**, *70*, 1023.

(29) Xu, S.; Mueser, Timothy C.; Marnett, Lawrence J.; Funk, Max O., Jr. *Structure*, *20*, 1490.

(30) Adams, P. D.; Afonine, P. V.; Bunkoczi, G.; Chen, V. B.; Davis, I. W.; Echols, N.; Headd, J. J.; Hung, L.-W.; Kapral, G. J.; Grosse-Kunstleve, R. W.; McCoy, A. J.; Moriarty, N. W.; Oeffner, R.; Read, R. J.; Richardson, D. C.; Richardson, J. S.; Terwilliger, T. C.; Zwart, P. H. *Acta Crystallogr., Sect. D* **2010**, *66*, 213.

(31) Brooks, B. R.; Brooks, C. L.; Mackerell, A. D.; Nilsson, L.; Petrella, R. J.; Roux, B.; Won, Y.; Archontis, G.; Bartels, C.; Boresch, S.; Caflisch, A.; Caves, L.; Cui, Q.; Dinner, A. R.; Feig, M.; Fischer, S.; Gao, J.; Hodoscek, M.; Im, W.; Kuczera, K.; Lazaridis, T.; Ma, J.; Ovchinnikov, V.; Paci, E.; Pastor, R. W.; Post, C. B.; Pu, J. Z.; Schaefer, M.; Tidor, B.; Venable, R. M.; Woodcock, H. L.; Wu, X.; Yang, W.; York, D. M.; Karplus, M. *J. Comput. Chem.* **2009**, *30*, 1545.

(32) Phillips, J. C.; Braun, R.; Wang, W.; Gumbart, J.; Tajkhorshid, E.; Villa, E.; Chipot, C.; Skeel, R. D.; Kalé, L.; Schulten, K. *J. Comput. Chem.* **2005**, *26*, 1781.

(33) Andersen, H. C. *J. Comput. Phys.* **1983**, *52*, 24.

(34) Huang, J.; MacKerell, A. D. *J. Comput. Chem.* **2013**, *34*, 2135.

(35) Darden, T.; York, D.; Pedersen, L. *J. Chem. Phys.* **1993**, *98*, 10089.

(36) Shao, Y.; Gan, Z.; Epifanovsky, E.; Gilbert, A. T. B.; Wormit, M.; Kussmann, J.; Lange, A. W.; Behn, A.; Deng, J.; Feng, X.; Ghosh, D.; Goldey, M.; Horn, P. R.; Jacobson, L. D.; Kaliman, I.; Khaliullin, R. Z.; Kuś, T.; Landau, A.; Liu, J.; Proynov, E. I.; Rhee, Y. M.; Richard, R. M.; Rohrdanz, M. A.; Steele, R. P.; Sundstrom, E. J.; Woodcock, H. L.; Zimmerman, P. M.; Zuev, D.; Albrecht, B.; Alguire, E.; Austin, B.; Beran, G. J. O.; Bernard, Y. A.; Berquist, E.; Brandhorst, K.; Bravaya, K. B.; Brown, S. T.; Casanova, D.; Chang, C.-M.; Chen, Y.; Chien, S. H.; Closser, K. D.; Crittenden, D. L.; Diedenhofen, M.; DiStasio, R. A.; Do, H.; Dutoi, A. D.; Edgar, R. G.; Fatehi, S.; Fusti-Molnar, L.; Ghysels, A.; Golubeva-Zadorozhnaya, A.; Gomes, J.; Hanson-Heine, M. W. D.; Harbach, P. H. P.; Hauser, A. W.; Hohenstein, E. G.; Holden, Z. C.; Jagau, T.-C.; Ji, H.; Kaduk, B.; Khistyaev, K.; Kim, J.; Kim, J.; King, R. A.; Klunzinger, P.; Kosenkov, D.; Kowalczyk, T.; Krauter, C. M.; Lao, K. U.; Laurent, A. D.; Lawler, K. V.; Levchenko, S. V.; Lin, C. Y.; Liu, F.; Livshits, E.; Lochan, R. C.; Luenser, A.; Manohar, P.; Manzer, S. F.; Mao, S.-P.; Mardirossian, N.; Marenich, A. V.; Maurer, S. A.; Mayhall, N. J.; Neuscamman, E.; Oana, C. M.; Olivares-Amaya, R.; O'Neill, D. P.; Parkhill, J. A.; Perrine, T. M.; Peverati, R.; Prociuk, A.; Rehn, D. R.; Rosta, E.; Russ, N. J.; Sharada, S. M.; Sharma, S.; Small, D. W.; Sodt, A. *Mol. Phys.* **2014**, *113*, 184.

(37) Shao, Y.; Molnar, L. F.; Jung, Y.; Kussmann, J.; Ochsenfeld, C.; Brown, S. T.; Gilbert, A. T. B.; Slipchenko, L. V.; Levchenko, S. V.; O'Neill, D. P.; DiStasio Jr, R. A.; Lochan, R. C.; Wang, T.; Beran, G. J. O.; Besley, N. A.; Herbert, J. M.; Yeh Lin, C.; Van Voorhis, T.; Hung Chien, S.; Sodt, A.; Steele, R. P.; Rassolov, V. A.; Maslen, P. E.; Korambath, P. P.; Adamson, R. D.; Austin, B.; Baker, J.; Byrd, E. F. C.; Dachsel, H.; Doerksen, R. J.; Dreuw, A.; Dunietz, B. D.; Dutoi, A. D.; Furlani, T. R.; Gwaltney, S. R.; Heyden, A.; Hirata, S.; Hsu, C.-P.; Kedziora, G.; Khalliulin, R. Z.; Klunzinger, P.; Lee, A. M.; Lee, M. S.; Liang, W.; Lotan, I.; Nair, N.; Peters, B.; Proynov, E. I.; Pieniazek, P. A.; Min Rhee, Y.; Ritchie, J.; Rosta, E.; David Sherrill, C.; Simmonett, A. C.; Subotnik, J. E.; Lee Woodcock Iii, H.; Zhang, W.; Bell, A. T.; Chakraborty, A. K.; Chipman, D. M.; Keil, F. J.; Warshel, A.; Hehre, W. J.; Schaefer Iii, H. F.; Kong, J.; Krylov, A. I.; Gill, P. M. W.; Head-Gordon, M. *Phys. Chem. Chem. Phys.* **2006**, *8*, 3172.

(38) Frisch, M. J.; Trucks, G. W.; Schlegel, H. B.; Scuseria, G. E.; Robb, M. A.; Cheeseman, J. R.; Scalmani, G.; Barone, V.; Mennucci, B.; Petersson, G. A.; Nakatsuji, H.; Caricato, M.; Li, X.; Hratchian, H. P.; Izmaylov, A. F.; Bloino, J.; Zheng, G.; Sonnenberg, J. L.; Hada, M.; Ehara, M.; Toyota, K.; Fukuda, R.; Hasegawa, J.; Ishida, M.; Nakajima, T.; Honda, Y.;

Kitao, O.; Nakai, H.; Vreven, T.; Montgomery Jr., J. A.; Peralta, J. E.; Ogliaro, F.; Bearpark, M. J.; Heyd, J.; Brothers, E. N.; Kudin, K. N.; Staroverov, V. N.; Kobayashi, R.; Normand, J.; Raghavachari, K.; Rendell, A. P.; Burant, J. C.; Iyengar, S. S.; Tomasi, J.; Cossi, M.; Rega, N.; Millam, N. J.; Klene, M.; Knox, J. E.; Cross, J. B.; Bakken, V.; Adamo, C.; Jaramillo, J.; Gomperts, R.; Stratmann, R. E.; Yazyev, O.; Austin, A. J.; Cammi, R.; Pomelli, C.; Ochterski, J. W.; Martin, R. L.; Morokuma, K.; Zakrzewski, V. G.; Voth, G. A.; Salvador, P.; Dannenberg, J. J.; Dapprich, S.; Daniels, A. D.; Farkas, Ö.; Foresman, J. B.; Ortiz, J. V.; Cioslowski, J.; Fox, D. J.; Gaussian, Inc.: Wallingford, CT, USA, 2009.

(39) Grimme, S.; Antony, J.; Ehrlich, S.; Krieg, H. *J. Chem. Phys.* **2010**, *132*, 154104.

(40) Grimme, S.; Ehrlich, S.; Goerigk, L. *J. Comput. Chem.* **2011**, *32*, 1456.

(41) Woodcock, H. L.; Hodošček, M.; Gilbert, A. T. B.; Gill, P. M. W.; Schaefer, H. F.; Brooks, B. R. *J. Comput. Chem.* **2007**, *28*, 1485.

(42) Rosta, E.; Woodcock, H. L.; Brooks, B. R.; Hummer, G. *J. Comput. Chem.* **2009**, *30*, 1634.

(43) Sievers, F.; Wilm, A.; Dineen, D.; Gibson, T. J.; Karplus, K.; Li, W. Z.; Lopez, R.; McWilliam, H.; Remmert, M.; Soding, J.; Thompson, J. D.; Higgins, D. G. *Mol. Syst. Biol.* **2011**, *7*, 539.

(44) Consortium, T. U. *Nucleic Acids Res.* **2014**, *42*, D191.

(45) Shirts, M. R.; Chodera, J. D. *J. Chem. Phys.* **2008**, *129*, 124105.

(46) Nina, M.; Beglov, D.; Roux, B. *J. Phys. Chem. B* **1997**, *101*, 5239.

(47) Souaille, M.; Roux, B. t. *Comput. Phys. Commun.* **2001**, *135*, 40.

(48) Kumar, S.; Rosenberg, J. M.; Bouzida, D.; Swendsen, R. H.; Kollman, P. A. *J. Comput. Chem.* **1992**, *13*, 1011.

(49) Rosta, E.; Nowotny, M.; Yang, W.; Hummer, G. *J. Am. Chem. Soc.* **2011**, *133*, 8934.

(50) Di Venere, A.; Horn, T.; Stehling, S.; Mei, G.; Masgrau, L.; González-Lafont, À.; Kühn, H.; Ivanov, I. *Biochim. Biophys. Acta, Mol. Cell Biol. Lipids* **2013**, *1831*, 1079.

(51) Toledo, L.; Masgrau, L.; Maréchal, J.-D.; Lluch, J. M.; González-Lafont, A. n. *J. Phys. Chem. B* **2010**, *114*, 7037.

(52) Rosta, E.; Hummer, G. *J. Chem. Theory Comput.* **2015**, *11*, 276.

(53) Pu, J.; Gao, J.; Truhlar, D. G. *Chem. Rev.* **2006**, *106*, 3140.

(54) Fernández-Ramos, A.; Miller, J. A.; Klippenstein, S. J.; Truhlar, D. G. *Chem. Rev.* **2006**, *106*, 4518.

(55) Isaksen, G. V.; Åqvist, J.; Brandsdal, B. O. *PLoS Comput Biol* **2014**, *10*, e1003813.

(56) Kazemi, M.; Himo, F.; Åqvist, J. *Proc. Natl. Acad. Sci. U.S.A.* **2016**.

(57) Tejero, I.; Garcia-Viloca, M.; González-Lafont, À.; Lluch, J. M.; York, D. M. *J. Phys. Chem. B* **2006**, *110*, 24708.

(58) Joshi, N.; Hoobler, E. K.; Perry, S.; Diaz, G.; Fox, B.; Holman, T. R. *Biochemistry* **2013**, *52*, 8026.

(59) Martin, J.; Baker, J.; Pulay, P. *J. Comput. Chem.* **2009**, *30*, 881.

(60) Oláh, J.; Mulholland, A. J.; Harvey, J. N. *Proc. Natl. Acad. Sci. U.S.A.* **2011**, *108*, 6050.

(61) Gaffney, B. J. *Acc. Chem. Res.* **2014**, *47*, 3588.

(62) Hammes-Schiffer, S. *J. Am. Chem. Soc.* **2015**, *137*, 8860.

(63) Soudackov, A. V.; Hammes-Schiffer, S. *J. Phys. Chem. Lett.* **2014**, *5*, 3274.

(64) Hatcher, E.; Soudackov, A. V.; Hammes-Schiffer, S. *J. Am. Chem. Soc.* **2007**, *129*, 187.

(65) Hatcher, E.; Soudackov, A. V.; Hammes-Schiffer, S. *J. Am. Chem. Soc.* **2004**, *126*, 5763.

(66) Hammes-Schiffer, S. *Energy Environ. Sci.* **2012**, *5*, 7696.

(67) Weinberg, D. R.; Gagliardi, C. J.; Hull, J. F.; Murphy, C. F.; Kent, C. A.; Westlake, B. C.; Paul, A.; Ess, D. H.; McCafferty, D. G.; Meyer, T. J. *Chem. Rev.* **2012**, *112*, 4016.

(68) Mayer, J. M. *Annu. Rev. Phys. Chem.* **2004**, *55*, 363.
(69) Reed, A. E.; Curtiss, L. A.; Weinhold, F. *Chem. Rev.* **1988**, *88*, 899.

Table of Contents Graphic